Korean J. Chem. Eng., 36(5), 688-700 (2019)
DOI: 10.1007/s11814-019-0262-6

pISSN: 0256-1115
eISSN: 1975-7220

Removal of cadmium from aqueous solutions using inorganic porous nanocomposites

Cătălin Ianăşi*, Mirela Picioruş*, Roxana Nicola*, Mihaela Ciopec, Adina Negrea**, Daniel Nižňanský***, Adél Len****, László Almásy*****,******, and Ana-Maria Putz*,†**

*"Coriolan Drăgulescu" Institute of Chemistry, Bv. Mihai Viteazul, No. 24, RO-300223, Timisoara, Romania
**Politehnica University of Timişoara, Faculty of Industrial Chemistry and Environmental Engineering, Vasile Pârvan Bd., No. 6, 300223, Timişoara, România
***Charles University in Prague, Faculty of Science, Albertov 6, 128 43, Prague, Czech Republic
****Centre for Energy Research, Hungarian Academy of Sciences, POB 49 Budapest 1525, Hungary
*****Wigner Research Centre for Physics, Institute for Solid State Physics and Optics, Hungarian Academy of Sciences, POB 49 Budapest 1525, Hungary
******State Key Laboratory of Environment-Friendly Energy Materials, Southwest University of Science and Technology, Mianyang, Sichuan 621010, China
(*Received 3 January 2019 • accepted 1 April 2019*)

Abstract−The present paper reports a one-pot synthesis of magnetic nanocomposites samples through acid catalyzed sol-gel method. Fe(III) acetylacetonate was used as precursor of the iron oxide phase: tetraethylortosilicate for the silica phase and polyvinyl alcohol (PVA, molecular mass 49000) as pore former. Different concentrations of Fe_2O_3 in composites matrices were prepared and studied ranging from 0% to 20%. All reactions took place in one pot at room temperature; the materials were subsequently heat treated at 300 °C, to ensure the crystallinity for the iron oxide having spinel structure, forming nanoparticles confined in the silica matrix. The materials were characterized using X-ray diffraction, small-angle neutron scattering, FT-IR spectroscopy, nitrogen adsorption, Mössbauer spectroscopy and magnetization measurements. The maximum value of room temperature saturation magnetization of ~54 emu/g and 0.11 kOe coercive field was achieved for the magnetic nanocomposite sample with 20% Fe_2O_3. The highest surface area of 680 m^2/g was obtained for the sample with 10% Fe_2O_3. The potential applicability of the obtained materials was studied for adsorption performance for cadmium in aqueous solutions. The Langmuir isotherm model described well the adsorption data, indicating monolayer adsorption of Cd(II) on the heterogeneous composite surface.

Keywords: Adsorption, Cadmium, Sol-gel, PVA, Iron Oxide

INTRODUCTION

Magnetic nanocomposites have become an important class of materials because of their favorable properties, finding use in different applications in medicine [1-3], electronics [4], catalysis [1,5], and removal of heavy metals [6,7]. Their properties should be tailored to ensure their dispersibility, preventing aggregation, oxidation and leaching. Magnetic nanoparticles under a certain size are superparamagnetic, and to remain in that state their agglomeration should be prevented [8]. Incorporation into inorganic silica or organic polymers is the most frequent procedure for preparing materials with magnetic properties suitable for applications. Various routes are known to synthetize iron-oxide containing composite silica materials. For applications such as adsorption, the porosity, surface area and surface-adsorbent interactions are the key factors to be controlled by choosing the suitable synthesis method [9,10]. Julian-Lopez et al. [9] showed that by encapsulating the magnetic nanoparticles in silica, the degree of dispersion improved, chemical stability of the material was enhanced and the toxicity reduced. To tailor these properties for obtaining the desired nanocomposites, Solinas et al. [11] used the sol-gel route for synthesis of magnetic nanocomposites using iron nitrate precursor, with subsequent thermal treatment at varying temperatures. Ullah et al. [12] prepared silica - iron oxide nanoparticle composites in a two-step method, targeting different ratios of iron oxide to silica. The majority of the magnetic nanocomposites were obtained by entrapment or by incorporation of previously prepared iron oxide nanoparticles into a silica or polymer matrix [5,13,14]. In the present study, we synthetized silica-based magnetic nanocomposites by using one-pot acid catalyzed sol-gel method, incorporating varied amount of superparamagnetic iron oxide phase. The obtained composite materials have been characterized for their morphology and magnetic properties, and tested for cadmium removal from aqueous media. Inorganic-organic composite materials prepared by sol-gel method have attracted great attention in separation science because they have high selectivity towards toxic metal ions [15-17].

Cadmium is a highly toxic pollutant which is being discharged into environment from natural and anthropogenic sources [16]. It is classified as carcinogenic, and exposure to cadmium is associated with prostate, pancreas and kidney cancers [16,18-20], or Alzheimer's and Parkinson's diseases [21]. Cadmium is often present in wastewater from industries such as dye and textile processing,

†To whom correspondence should be addressed.
E-mail: lacramaanamaria@yahoo.com

pesticides, printing and photographic industries and pigment manufacture [21,22]. Such processes release heavy metals into the industrial wastewater, thereby posing a hazard to the environment. Consequently, intensive research is going on to develop suitable adsorbents for removal of hazardous pollutants from the contaminated environment [23,24]. Heavy metals are generally refractory and cannot be degraded or readily detoxified biologically [15]. For the adsorption process, the adsorption properties of the used materials of the adsorbents are very important [20]. For example, Bystrzejewski et al. studied the efficiency of carbon-encapsulated magnetic nanoparticles for Cd^{2+} removal and found that the adsorption capacity was 1.77 mg/g for 20 mg/L initial metal concentration, using 50 mg of adsorbent material [25]. Similar studies by Phuengprasop et al. on municipal sludge modified with iron oxide obtained an adsorption capacity for this kind of material of 14.7 mg/g, for 1 g/L of adsorbent material and 20 mg/L initial Cd^{2+} concentration [26]. Zhang et al. investigated $Ni@Mg(OH)_2$ core-shell composite nanostructures as metal ion adsorbent and achieved 45.02 mg/g adsorption capacity, using 200 mg adsorbent material and initial Cd^{2+} concentration was 100 mg/L [27]. Areca waste was also used as metal biosorbent, and the highest value of Langmuir maximum uptake for Cd^{2+} was found to be 1.12 mg/g, using 0.010 g/L adsorbent material and metal initial concentration was 8 mg/L [28].

In the present study, the potential applicability of silica based inorganic composite materials was studied for adsorption performances for cadmium in aqueous solutions.

EXPERIMENTAL

1. Preparation of Composites

All the composite samples were obtained by the acidic catalyzed sol-gel method. Reagent-grade chemicals, TEOS (Tetraetoxyortosilicate), PVA (Polyvinyl alcohol, with molecular mass of 49000) and $Fe(acac)_3$ (iron III acetylacetonate) were used. The molar ratio of the reactants was $TEOS : H_2O : PVA : Fe(acac)_3 : CH_3OH : HNO_3 = 1 : 10 : 1.89*10^{-5} : x : 18 : 0.01$. Here x stands for the molar amount of $Fe(acac)_3$ which was set as 0; 0.1; 0.15 and 0.2.

2.04 g of PVA was dissolved in 90 mL of distilled water, stirred at 85 °C for two hours and next completed, up to 100 mL with water. The silica sol was obtained from 23.7 g TEOS, 0.07 g HNO_3 and 15.14 g distilled water, and stirred for 30 minutes. Next, 5 g of the previously obtained PVA solution was added and stirred for another 15 minutes. Different amounts of $Fe(acac)_3$ were dissolved in 63.91 g of methanol and stirred at 55 °C for 15 minutes. Then they were poured into a silica sol-PVA mixture and stirred for 15 minutes at 55 °C. The 0-NC sample (no iron oxide content) was also stirred for 15 minutes at 55 °C, for comparison purposes. A gel was formed after four days and was subsequently dried at 60 °C. The resulting composite samples were thermally treated at 300 °C. Samples are denoted as: 0-NC (no iron oxide content) and 10-NC, 15-NC, 20-NC (with different content of iron oxide).

2. Characterization

The infrared spectra were recorded using a JASCO FT/IR-4200 instrument. Scanning electron microscopy analysis (SEM) FEI Quanta FEG 250 coupled with EDX was used to characterize the morphology of the materials. The surface area and porosity were determined by Nova 1200e Quantachrome apparatus. The materials were degassed in vacuum at 100 °C for four hours prior the measurements. X-ray diffraction patterns were recorded over $10^o < 2\theta < 80^o$ with a Panalytical X'Pert Pro MPD diffractometer. Small-angle neutron scattering (SANS) measurements were performed on the *Yellow Submarine* diffractometer installed at the cold neutron beamline at the Budapest Neutron Centre [29]. At the time of the experiment the cold source was not in operation, and the measurements were performed with thermal neutrons using wavelengths 4.4 and 10.2 Å, in order to cover a q-range 0.005-0.42 $Å^{-1}$. Samples were measured in powder form at room temperature. Analysis was performed by fitting analytical models to the experimental data, using a home-made software. Mössbauer spectra were recorded in the transmission mode with ^{57}Co diffused into a Rh matrix as a source moving with constant acceleration. Magnetic properties were measured in AC (50 Hz) field of 5 kOe amplitude by means of a home-made induction magnetometer [30].

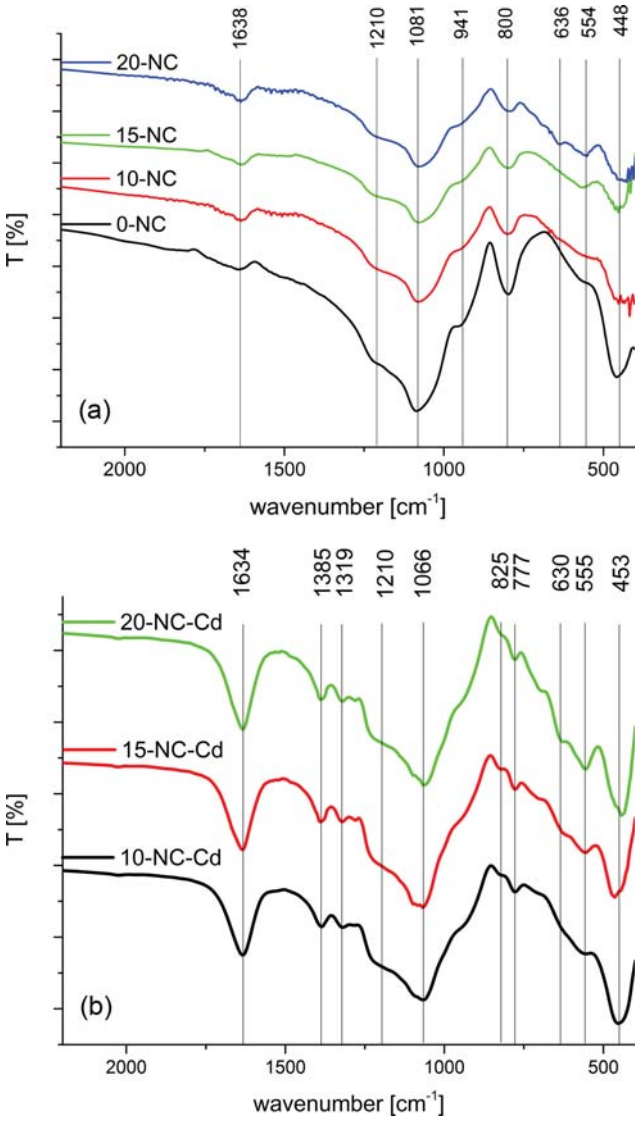

Fig. 1. FT-IR spectrum of nanocomposites with the increase of iron concentration: (a) without Cd; (b) with Cd.

Table 1. FT-IR bands wavenumber and assignment of nanocomposites

Nanocomposites without cadmium		Nanocomposites with cadmium	
Wavenumber (cm^{-1})	Assignment	Wavenumber (cm^{-1})	Assignment
3442	(O-H)	3425	(O-H)
1638	δ(O-H)	1634	δ(O-H)
		1385; 1319	NO_3^-
1210	δ(CH)+ν(C-CH_3) and/or ν(C-CH_3)+ν(C C), TO Si-O-Si	1210	TO Si-O-Si
1081	νSi-O-Si, δ(O-H), ν(C-O)	1066	νSi-O-Si, δ(O-H), ν(C-O); Si-O-Cd
941	νs (C-O), νSiOH	940	νs (C-O), νSiOH
		825	Cd-O
800	νs Si-O-Si, CγCOFe	777	νs Si-O-Si, CγCOFe; Si-O-Fe
636	γw(OH), Fe-O	630	γw(OH), Fe-O
554	FeOC	555	FeOC
448	δO-Si-O, FeO	453	δO-Si-O, FeO

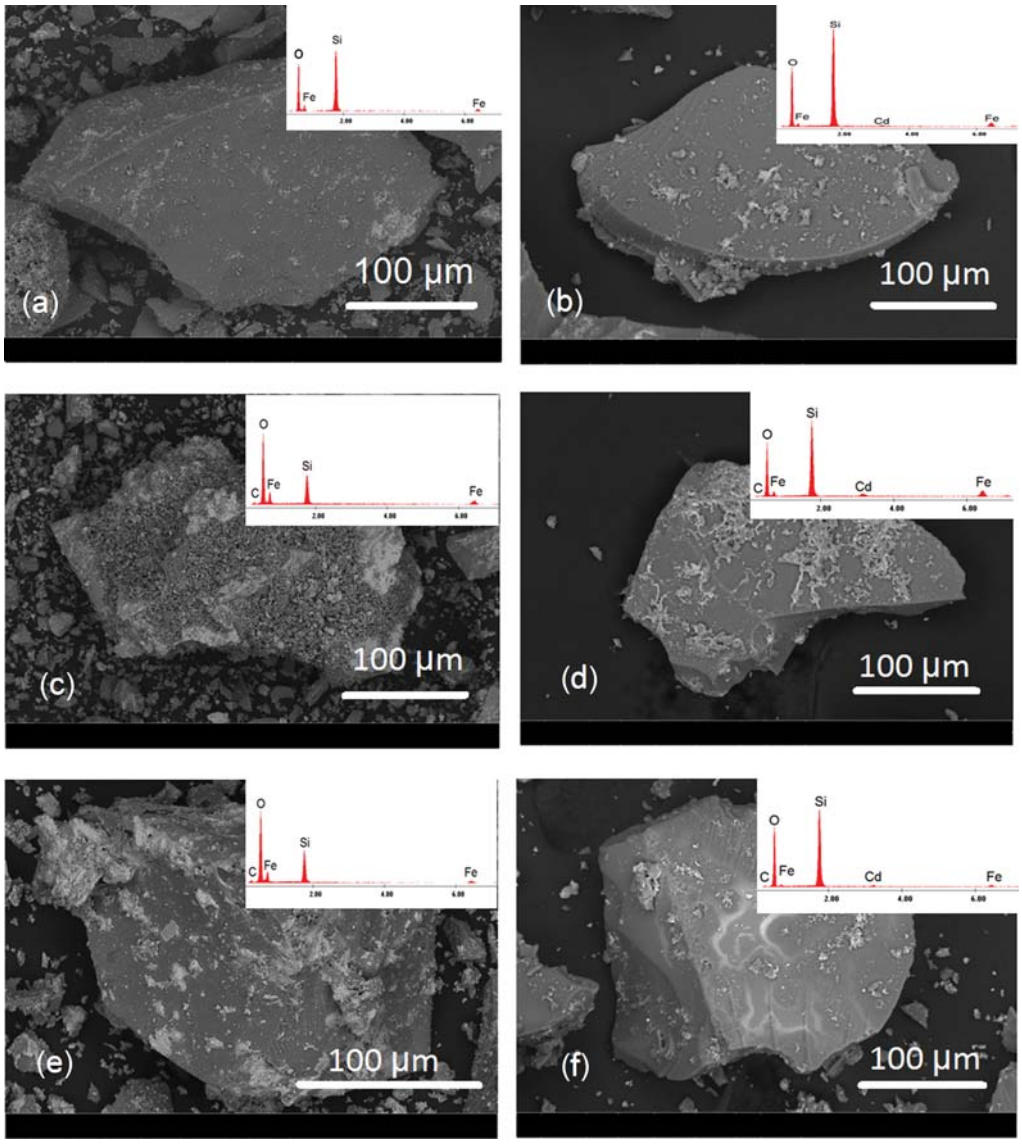

Fig. 2. SEM and EDAX images of nanocomposites with the increase of iron concentration: (a) 10-NC, (b) 10-NC-Cd, (c) 15-NC, (d) 15-NC-Cd, (e) 20-NC, (f) 20-NC-Cd.

RESULTS AND DISCUSSION

1. FT-IR Spectroscopy

Fig. 1(a) and Fig. 1(b) show the IR spectra of the calcinated nanocomposites in SiO_2-PVA-Fe_2O_3 system with different iron concentration before and after sorption of cadmium. We can observe that almost all the characteristic bands for silica matrix are encountered in this spectrum. The specific bands of silica are found at 448, 800, 941, 1,081 and 1,210 cm^{-1}. The specific bands of iron oxide are found in the interval 400-800 cm^{-1}, the majority of them being superposed on the vibrations of silica, except bands at 554 and 636 cm^{-1} which are characteristic for iron oxide [31-33]. All bands of the FTIR spectra are collected and assigned in Table 1.

Increasing the iron concentration, no visible band shifts occurs, but the intensities of the following bands change significantly: 1,081, 800, 636 and 554 cm^{-1}. From this, it may be perceived that with lower quantity of iron oxide introduced into sample, the specific bands for silica are more intense. In the case of 0-NC sample, another band at 3,700 cm^{-1} attributed to non-hydrogen bonded OH groups can be observed.

After cadmium adsorption, certain changes in the spectra were observed. The majority of bands characteristic to Si-O-Si were shifted, mainly due to the breakage of the OH after binding with cadmium but also with iron. Two specific bands, due to the cadmium adsorption, are seen at 1,385 cm^{-1} and 825 cm^{-1}. The first one is specific for the NO_3^- anions and indicates the presence of cadmium nitrate in the sample [34]. The second band at 825 cm^{-1}, indicates the interaction of cadmium with silica matrix and can be attributed to CdO bond on the surface [35,36]. The band at 777 cm^{-1}, attributed to Si-O-Fe [37] is slightly shifted after Cd adsorption.

2. SEM and EDAX

In Fig. 2 the SEM images before and after cadmium adsorption are presented. In the insets the EDAX spectra are shown. The results indicate that after the cadmium was introduced, the amorphous phase of samples was reduced, so a more compact surface is observed. The images indicate an overlaid plate-like structure. Overall, the dimensions of aggregates obtained are decreasing with the increase of iron concentration from 300 μm to 200 μm. The EDAX measurements confirmed the presence of Cd in the materials visible also from FT-IR spectroscopy.

3. Surface Area and Porosity

Nitrogen adsorption/desorption isotherms with and without adsorbed cadmium are presented in Fig. 3(a) and Fig. 3(b). Sample 0-NC exhibits a type IV-a isotherm with H4 hysteresis loop, characteristic for mesoporous materials with small percentage of micro porosity. In case of samples 10-NC, 15-NC and 20-NC the isotherms present a concave allure at low P/Po values, indicating a type I (IUPAC) isotherm or Langmuir isotherm. These isotherms present in most cases only micropores having a small external surface area [38].

In case of samples after the cadmium was adsorbed, some changes were observed. The isotherms for sample 10-NC-Cd and 15-NC-Cd indicate a type I isotherm and the sample 20-NC-Cd show a type IVa with a H4 hysteresis loop.

In Fig. 4(a) and Fig. 4(b), the pore size distributions of materials calculated by DFT method are illustrated. The calculations indicate the clear presence of microporous material with high internal surface area and some wider micropores at the limit of mesoporosity as suggested by the isotherm shape. For the sample 0-NC, the results show only narrow micropores of 2.3 nm diameter. For the composite samples, the results indicate the majority of micropores smaller than 2 nm, and some wider ones at 2.5 nm growing in quantity with the increase of the iron oxide concentration.

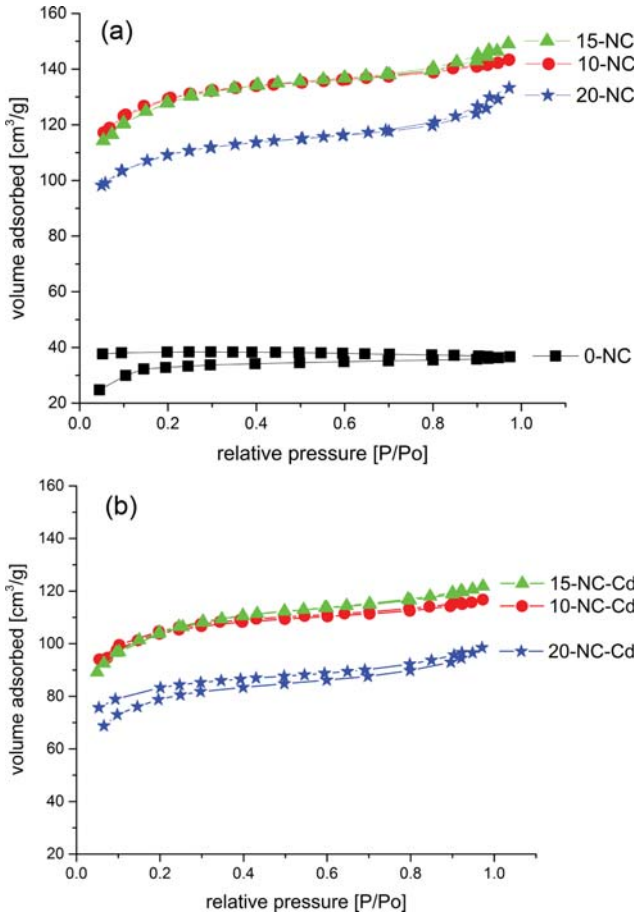

Fig. 3. N_2 adsorption-desorption isotherms for the composite samples: (a) without Cd; (b) with Cd.

For the samples with adsorbed cadmium we observed a small increase in size for all samples. In Table 2 are collected the textural parameters of the studied samples.

The specific surface area was evaluated by BET (Brunauer Emmet Teller) equation. The total pore volume was determined at 0.99 relative pressure by the Gurvischt rule. The micropore volume was calculated by Alpha-S method [39].

The sample 15-NC adsorbed about 0.231 cm^3/g of N_2 presenting the biggest total pore volume with a surface area of 649 m^2/g. Following Alpha-S method we observed that the sample 10-NC adsorbed more gas possessing the biggest micropore volume and the biggest surface area of 680 m^2/g. Introducing a smaller amount of iron in the silica sample, a higher surface area could be obtained (sample 10-NC). With the increase of concentration of iron oxide in silica (15-NC and 20-NC), the number of pores started to decrease, or be filled with the iron oxide, thus resulting in a slightly

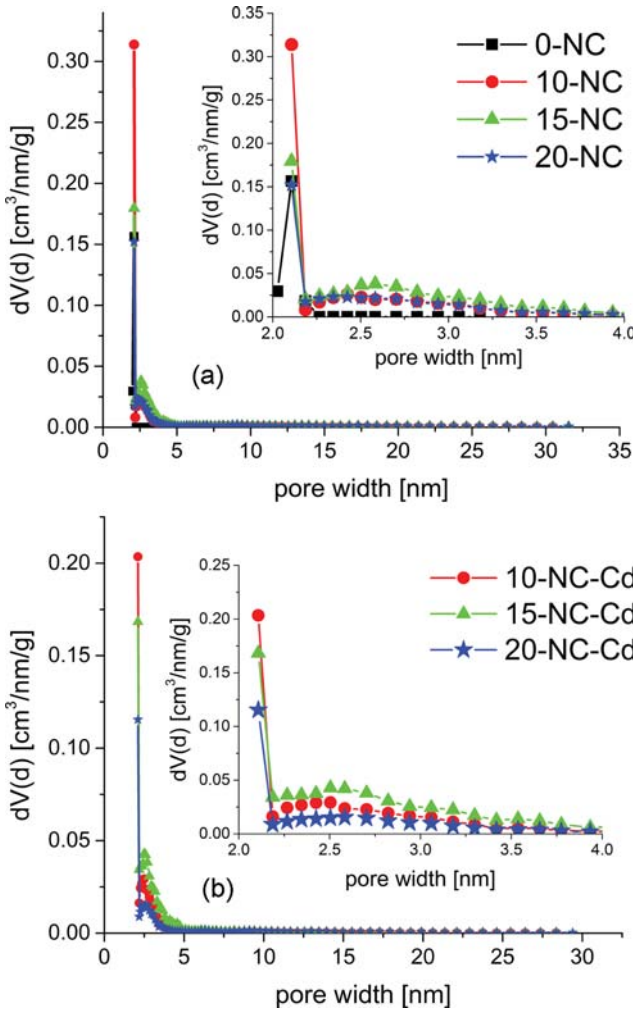

Fig. 4. Pore size distribution by DFT method for the samples with the increase of iron concentration: (a) without Cd; (b) with Cd.

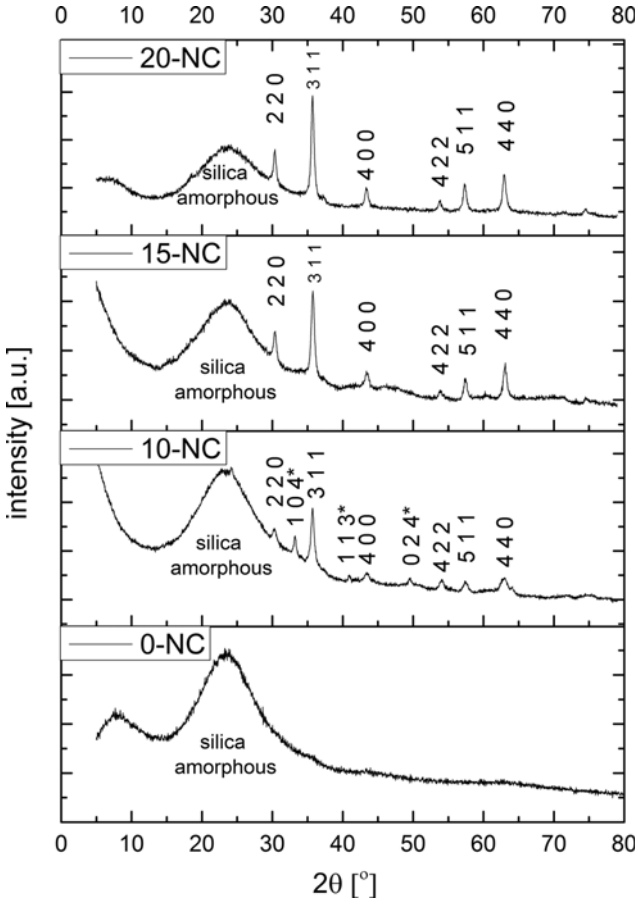

Fig. 5. Powder X-ray diffraction (XRD) patterns of the nanocomposite particles with the increase of iron concentration. The stronger peaks belong to maghemite; the 104, 113 and 024 reflections are from hematite.

smaller surface area, pore size distribution and total pore volume. The 10-NC, 15-NC and 20-NC samples present 75% microporosity. FHH method shows an increase of rugosity with the increase of iron concentration.

In case of samples with adsorbed cadmium we observed a decrease of the surface area, indicating that a part of pores is filled with cadmium. The rugosity of samples indicates also a smoother surface when cadmium was added. The SEM images, Fig. 2, show also a more compact surface in case of samples with adsorbed cadmium.

4. X-ray Diffraction

Powder X-ray diffraction (XRD) patterns of the nanocomposite particles with different iron concentration are shown in Fig. 5. The diffractograms show the peaks characteristic for maghemite crystal structure [40] at 30.3, 35.7, 43.4, 53.7, 57.3 and 62.9 degrees 2θ with an additional broad peak between 15 and 30°, belonging to amorphous silica. For the 10-NC sample, the presence of hematite [41] is put in evidence by the peak located at 33 degrees, corre-

Table 2. Textural parameters of samples with the increase of iron concentration, before and after cadmium adsorption

Sample	S_{BET} [m²/g]	S_L [m²/g]	$S_{t\text{-}plot}$ [m²/g]	d_{DFT} [nm]	d_{BJH} [nm]	VTP [cm³/g]	Alpha-S [cm³/g]	d_s FHH
0-NC	105	157	95	2.3	3.4	0.056	0.046	2.95
10-NC	482	680	363	1.9	3.1	0.222	0.182	2.90
10-NC-Cd	381	502	339	2.1	3.3	0.181	0.146	2.96
15-NC	475	649	355	1.9	3.1	0.231	0.175	2.86
15-NC-Cd	370	487	331	2.1	3.3	0.189	0.141	2.95
20-NC	406	571	304	1.9	3.1	0.206	0.151	2.83
20-NC-Cd	284	380	248	2.1	3.3	0.153	0.105	2.93

Table 3. X-ray diffraction results of samples with the increase of iron concentration

Sample	Composition	Crystallite size [nm] *Scherrer equation*: $D=K\lambda/(\beta\cos\theta)$
0-NC	Amorphous	N/A
10-NC	Maghemite (γ-Fe_2O_3)/ Hematite (α-Fe_2O_3)	23/31
15-NC	Maghemite (γ-Fe_2O_3)	28
20-NC	Magnetite (Fe_3O_4)/ Maghemite (γ-Fe_2O_3)	30/31

sponding to diffraction with Miller index 104, and also by two weak lines with Miller indexes at 113 and 024. Sample 0-NC shows only the amorphous broad peak specific to glassy silica. The Scherrer equation was used to determine the crystalline size of materials, see Table 3.

For all samples, the results indicate an increase of crystallite size when iron oxide is introduced. The appearance of hematite, for sample 10-NC, could be due to the increase of nanoparticles crystallite size to 31 nm [42]. The presence of broad peak of amorphous silica beside the peaks specific to iron oxide indicates that the samples were coated efficaciously on the surface of the nanoparticles. Magnetite and maghemite phases can hardly be separated by diffraction [43], but the presence of both was revealed by Mössbauer spectrometry.

5. Small-angle Neutron Scattering (SANS)

Small-angle scattering is a powerful method of structure analysis of amorphous and semicrystalline materials, giving information on the length scales roughly from 1 to 100 nm. At this resolution, scattering is sensitive to the differences of scattering length densities, called contrast. The 0-NC sample is dry silica gel, consisting of agglomerated silica particles and air. The primary units are the small particles formed during the polycondensation process [44]; their agglomerates form a solid network with grain sizes of several hundreds of nanometers. The three silica - iron oxide com-

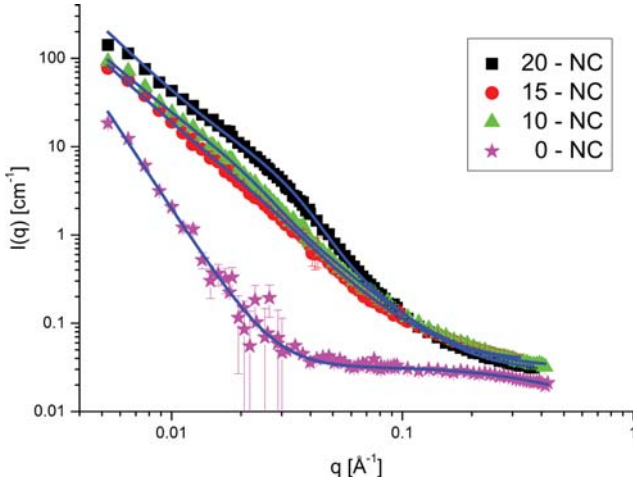

Fig. 6. Small-angle neutron scattering data of the silica nanocomposites.

Table 4. Structural parameters obtained by fitting Eq. (1) to SANS data of the nanocomposites

Sample	Rg, Å	p	χ^2
0-NC	4.9±0.2	3.99±0.02	1.53
10-NC	103.3±2.2	2.33	5.98
15-NC	74.5±1.7	2.38	4.71
20-NC	66.6±0.2	2.56	5.62

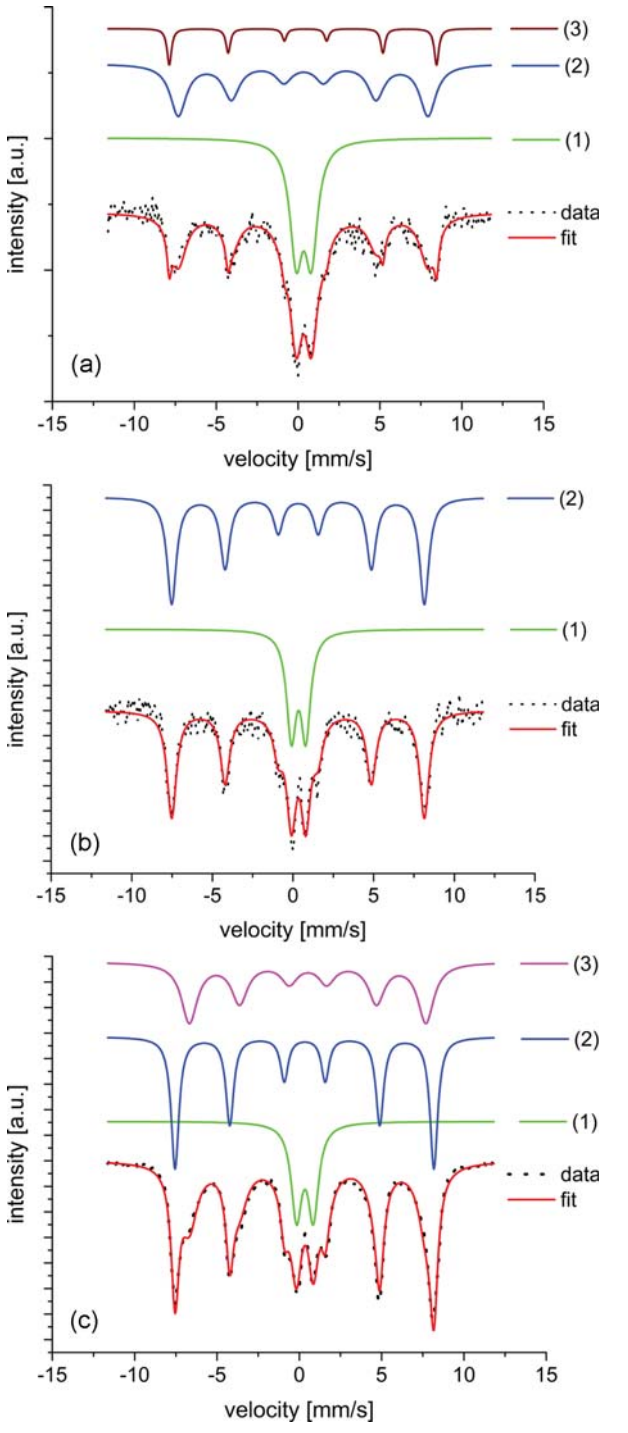

Fig. 7. Mössbauer spectra of magnetic nanocomposites. (a) 10-NC, (b) 15-NC and (c) 20-NC.

posite samples have three-phase morphology, and the scattering generally contains a contribution from all phase boundaries. The interpretation is facilitated when one or two components prevail and dominate the scattering pattern. The scattering data of the four samples is shown in Fig. 6. The xerogel and the composite samples show markedly different pictures: the 0-NC sample shows a distinct power-law part at small q, which is characteristic of sharp phase boundaries, and a broad maximum centered at zero and extending beyond the maximum q reached in the measurement. The composite samples show a much stronger scattering intensity, which can be attributed to the presence of the iron oxide nanoparticles. The curvature at q=0.03 $Å^{-1}$ indicates the presence of inhomogeneity of characteristic 20 nm, and can be identified with the iron oxide particles embedded in the silica matrix.

The scattering curves of all samples could be modelled by Eq. (1), frequently used to describe systems with complex morphology having multiple levels of characteristic sizes [45,46]:

$$I(q) = Aq^{-p} + B\exp\left(\frac{-qRg}{3}\right) + bg \quad (1)$$

Here the first term describes the scattering from the large silica and silica - iron oxide agglomerated particles, and the second term is the Guinier equation [47] that describes the size of the primary silica particles in the 0-NC sample and the iron oxide nanoparticles in the composite samples. In the composite samples the strong scattering from the iron oxide nanoparticles masked the signal from the small silica beads. In this model, the Guinier radius gives an estimate of the average size of the otherwise polydisperse iron oxide crystallites. The results of modelling are shown in Table 4.

The SANS data show the two-level structure generally present in dry xerogel materials, consisting of primary units and their agglomerates [48-51], and the presence of finite size nanoparticles of average sizes 20-30 nm.

6. Mössbauer Spectra

Mössbauer spectra are shown in Fig. 7. They can be decomposed into doublets and sextets (Table 5). The doublets represent the iron in magnetically disordered state like paramagnetic, superparamagnetic or amorphous state, while the sextets correspond to magnetically ordered state at ferromagnetic, antiferromagnetic or ferrimagnetic.

From Table 5, the amount of magnetically disordered phase decreases from 42% to 20% due to increase of iron oxide concentration and formation of larger crystals that are magnetically ordered. In case of sample 15-NC only maghemite phase was formed. Sample 10-NC shows besides the maghemite phase also the hematite phase with amount of 9%. The sample 20-NC contains magnetite having almost the same amount as maghemite.

Mössbauer spectra show that with the increase of iron concentration, oxidation is not complete and magnetite starts forming; also, hematite was present in the 10-NC sample [52].

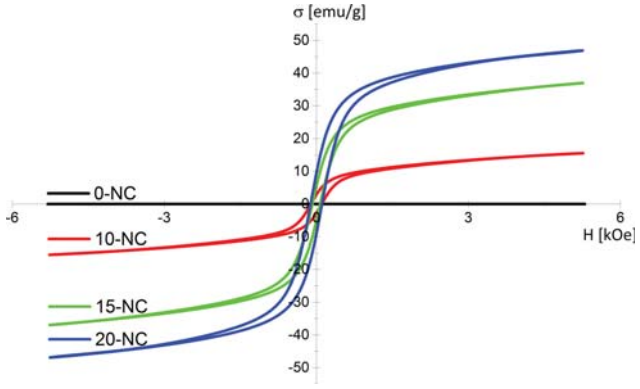

Fig. 8. Magnetization curves of nanocomposites obtained at room temperature.

Table 6. Room temperature magnetization parameters

Sample	Saturation magnetization [emu/g]	Remanent magnetization [emu/g]	Coercive field [kOe]
0-NC	N/A	N/A	N/A
10-NC	29.71	2.88	0.108
15-NC	46.77	5.24	0.076
20-NC	54.19	9.25	0.115

7. Magnetization

The room temperature magnetization curves are presented in Fig. 8, and the derived data are collected in Table 6.

The curves show a small hysteresis, indicating predominantly superparamagnetic behavior of the composite samples. The data shows that the saturation magnetization is increasing with the in-

Table 5. Room temperature Mössbauer parameters

Sample	Isomer shift δ	Quadrupole splitting ΔEQ	Hyperfine field BHf	Relative area [%]	Attribution
0-NC	N/A	N/A	N/A	N/A	-
10-NC	(1)=0.347	(1)=0.923	N/A	42	Fe(III) in magnetically non-ordered phase
	(2)=0.324	(2)=−0.034	(2)=47.387	49	Maghemite
	(3)=0.375	(3)=−0.158	(3)=50.729	9	Hematite
15-NC	(1)=0.347	(1)=0.891	N/A	33	Fe(III) in magnetically non-ordered phase
	(2)=0.317	(2)=−0.012	(2)=48.684	67	Maghemite
20-NC	(1)=0.342	(1)=1.014	N/A	20	Fe(III) in magnetically non-ordered phase
	(2)=0.324	(2)=−0.018	(2)=48.865	41	Maghemite
	(3)=0.517	(3)=−0.021	(3)=44.634	39	Magnetite

crease of iron content, reaching 54 emu/g for the sample with 20% iron content. Same increasing trend is seen for the remanent magnetization. The coercive field was the smallest for the sample 15-NC, which presents only maghemite phase.

8. Adsorption Studies

To determine the adsorption performance of the new synthesized materials, the effect of initial concentration of Cd(II) solution onto the materials adsorption capacity was studied. Samples of 0.1 g of dry composite beads were mixed with 25 mL Cd(II) solutions, at concentrations between 5 and 40 mg/L, and stirred for 120 minutes at 25 °C in a Julabo SW23 thermostatic and shaking water bath with a stirring speed of 200 rpm. Because at pH~8, precipitation of cadmium hydroxides occurs, for the present experiment pH was kept in range 4-6. The pH of solutions was measured using CRISON MultiMeter MM41 with a glass electrode, which had been calibrated using various buffer solutions. Analysis of residual cadmium content into the solutions was by atomic absorption spectrometry using a Varian SpectrAA 280 FS atomic absorption spectrometer. The equilibrium adsorption capacity and adsorption isotherm equations are given in Table 7.

8-1. The Influences of the pH and Contact Time and Temperature on the Capacity of Adsorption

The pH of the solutions represents the most significant variables with an important effect on the affinity of a material for a certain ion. This influence of the pH is related to the form of the metallic ion from the solution and to the functional group from the surface of the extracting composite material. For the adsorption process, the pH of Cd^{2+} solutions was set in the 4-6 pH interval, being considered from literature studies [55], as the pH interval in which the most H^+ ions are released and further adsorbed on the three composite materials surfaces, to Si-O and to Fe-O groups. The composite with 20% Fe, contains more functional groups, and a better sorption capacity of this composite for the Cd^{2+} ions has been observed. Therefore, we may presume that the Fe-O group has an increased role in Cd^{2+}, comparatively with Si-O group. Different literature studies tried to enrich and to give new explanations of the adsorption mechanism. One way to explain the adsorption mechanism is by measuring the zeta potential [27]. The electrostatic attraction coming from the surface charges of particles is another important factor deciding the adsorption behavior [27,56]. The surface charges are usually varied with the change of pH value, so the zeta potential of the nanocomposite at different pH conditions should be also analyzed in adsorption studies. For example, the zeta potential is positive at low pH values, and by increasing pH value the zeta potential gradually becomes negative, while pH value increases to 6.5, for the analyzed nanocomposite, in Zhang et al., 2015 study. This fact that negative charges are present on the surface of the nanocomposite helps enhance the adsorption capacity for heavy metal ions through additional electrostatic attraction [27]. The solution pH has a significant effect on the uptake of metal, since it determines the surface charge of the adsorbent and the degree of ionization and speciation of the adsorbate. It is very common that acidic solution hinders metal uptake because of high concentration of H^+ ions competing with metal ions due to the protonation of various functional groups on the surface of the adsorbents. With increasing pH, the competition from the hydrogen ions decreased and the positively charged ions could be adsorbed at the negatively charged sites on the adsorbent [57]. In the cases of processes of adsorption in dynamic regime (on column), the breakthrough capacity is measured, as well [57].

The contact time and temperature of the adsorption process are other important factors for the evaluation of the material affinity for the Cd^{2+} ions. To establish the influences of the contact time and of the temperature on the capacity of adsorption of the functionalized material, 0.1 g of material was mixed with 25 mL Cd^{2+} solution (10 mg/L), prepared from a $Cd(NO_3)_2$ standard solution 1,000 mg/L (Merck). Different stirring times were used--5, 15, 30, 45, 60, 90 and 120 minutes--by using a water bath Julabo SW23 type (with thermostat and shaker) at different temperatures (298 K, 308 K and 318 K). The samples were shaken at 200 rot/min. In all cases, the samples were filtered and the residual concentration of Cd^{2+} was evaluated by atomic adsorption spectrometry (Varian SpectrAA 280 FS). The adsorption capacity of the material, q (mg/g) was calculated as previously presented in Table 7.

8-2. Kinetics of the Adsorption Process

The kinetics of the Cd^{2+} adsorption on the three composites was studied by using two kinetics model equations: the equation of pseudo-first-order proposed by Lagergren and the kinetic equa-

Table 7. Quantities and equations for equilibrium adsorption isotherms

Adsorption capacity	$q_e = \frac{(C_0 - C_e)V}{m}$	q_e - maximum absorption capacity (mg/g) C_0 - initial concentration of Cd(II) in solution (mg/L) C_e - equilibrium concentration of Cd(II) in solution (mg/L) V - volume of the aqueous solution with Cd(II) content (L) m - mass of the adsorbent (g)	
Langmuir isotherm	$q_e = \frac{q_L K_L C_e}{1 + K_L C_e}$	q_e - maximum absorption capacity (mg/g) C_e - equilibrium concentration of Cd(II) in solution (mg/L) q_L - Langmuir maximum adsorption capacity (mg/g) K_L - Langmuir constant	[53]
Freundlich isotherm	$q_e = K_F C_e^{1/n_F}$	q_e - maximum absorption capacity (mg/g) C_e - equilibrium concentration of Cd(II) in solution (mg/g) K_F and n_F - characteristic constants related to the adsorption capacity and the intensity of adsorption	[54]

tion of the pseudo-second order.

The pseudo-first-order equation can be expressed as follows:

$$\frac{dq_t}{dt} = k_1(q_e - q_t) \quad (2)$$

where q_e and q_t are the adsorbed amounts of adsorbent per unit mass of material at equilibrium and time t, respectively, and k_1 is the rate constant for pseudo-first-order adsorption model. The q_t at different times t can be determined by the following pseudo-first-order kinetic equation after integrating:

$$\ln(q_e - q_t) = \ln q_e - k_1 t \quad (3)$$

The kinetic model of pseudo-second order may be presented by using the following equation:

$$\frac{dq_t}{dt} = k_2(q_e - q_t)^2 \quad (4)$$

where k_2 is the rate constant for the pseudo-second-order adsorption. By the linearization of this equation, the following relation is obtained:

$$\frac{t}{q_t} = \frac{1}{k_2 q_e^2} + \frac{t}{q_e} \quad (5)$$

For the modelling of the experimental data, the linear forms of the two models were used. The kinetic constant for the pseudo-first-order is calculated from the linear representation of $\ln(q_e - q_t)$ function of time, and the kinetic constant for the pseudo-second order, was estimated from the linear representation of t/q_t function of time. Based on the values of the resulting constants and of the obtained regression coefficients (R^2), the kinetic model that describes best the adsorption process can be established. All the obtained experimental data for the Cd^{2+} adsorption process for all the three composites materials at all three studied temperatures were best fitted by the pseudo-second-order kinetic model. The graphical representation of these curves is presented in Fig. 9, and the values of the kinetics parameters are presented in Table 8.

8-3. Thermodynamics of the Adsorption Process

Since with the temperature increases, the adsorption capacity of the material also increases, it can be concluded that the adsorption process is endothermic. The specific thermodynamic parameters were calculated: the Gibbs free energy (ΔG^0), the free enthalpy (ΔH^0) and the free entropy (ΔS^0) by using the followings equations:

$$\Delta G^0 = -RT\ln K_c \quad (6)$$

$$\text{where: } K_d = \frac{C_{Ae}}{C_e} \quad (7)$$

$$\text{and } \log K_d = \frac{\Delta S^0}{2.3R} - \frac{\Delta H^0}{2.303RT} \quad (8)$$

where R is the gas constant, K_d is the equilibrium constant, T is the temperature (K), C_{Ae} is the equilibrium concentration Cd^{2+} on adsorbent (mg/L), and C_e is the equilibrium concentration of Cd^{2+} in the solution (mg/L).

In all the cases of Cd^{2+} adsorption on the three synthetized composites materials, the thermodynamic parameters were calculated from the slope and the intercept, by using the linear representation of $\ln K_d$ function of 1/T (Fig. 10). The ΔG^o, ΔH^o and ΔS^o values are collected in Table 9.

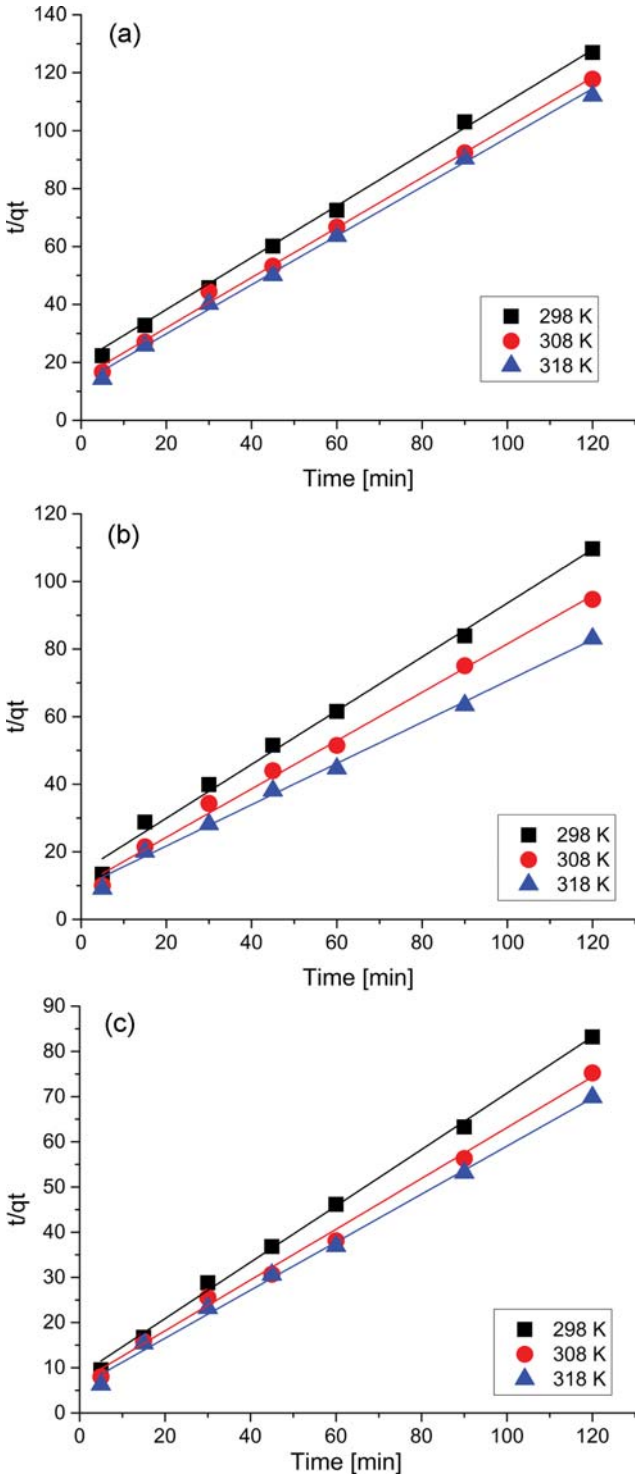

Fig. 9. Lagergren pseudo-second order kinetic model of Cd^{2+} adsorption on the nanocomposites materials (a) 10-NC, (b) 15-NC, (c) 20-NC.

From the thermodynamic studies it resulted that negative values of the Gibbs free energy (ΔG^o) were obtained, at all the studied temperatures, indicating that the adsorption process is sponta-

Table 8. Kinetic parameters for adsorption of Cd(II) onto materials

Temp (K)	$q_{e,exp}$, mg/g	Pseudo-first-order kinetic model				Pseudo-second-order kinetic model			
		$q_{e,calc}$, mg/g	k_1, min^{-1}	R^2	χ^2	$q_{e,calc}$, mg/g	k_2, min^{-1} $(mg/g)^{-1}$	R^2	χ^2
10-NC									
298	0.95	0.45	0.0113	0.8127	0.32	1.12	0.89645	0.9901	0.017
308	1.02	0.52	0.0136	0.8292	0.41	1.15	0.86443	0.9967	0.022
318	1.07	0.62	0.0153	0.8541	0.44	1.18	0.84654	0.9953	0.012
15-NC									
298	1.09	0.66	0.0091	0.914	0.65	1.26	0.7957	0.9939	0.027
308	1.27	0.72	0.0126	0.9329	0.78	1.31	0.7155	0.9946	0.031
318	1.44	0.82	0.0266	0.9456	0.85	1.63	0.6108	0.9906	0.033
20-NC									
298	1.44	0.92	0.0109	0.9057	0.23	1.50	0.6237	0.9949	0.021
308	1.59	1.01	0.0162	0.8475	0.82	1.67	0.5621	0.9935	0.037
318	1.72	1.02	0.0232	0.9020	0.28	1.81	0.5314	0.9962	0.011

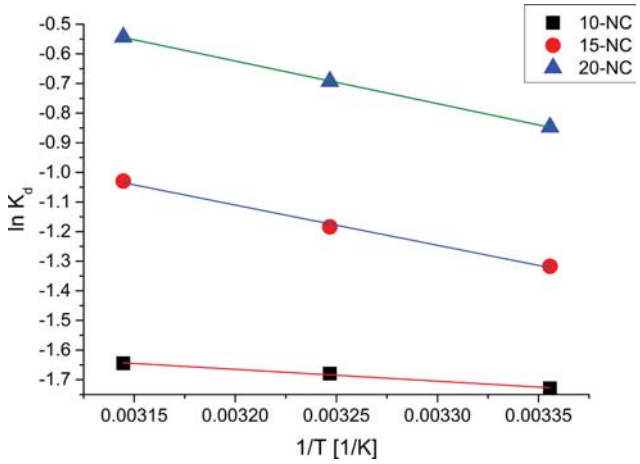

Fig. 10. Van't Hoff plots for the adsorption of Cd^{2+}.

neous [58]. The values for the free Gibbs free energy are decreasing from −2,412 to −2,796 kJ/mol, as the temperature is increasing from 298 K to 318 K. This indicates that the Cd^{2+} adsorption process is spontaneous. The decrease of the free energy indicates the existence of a reduced driving force and the adsorption process is influenced by temperature. The positive value of the standard entropy (ΔS^o) indicates a decrease of the free space at the solid-liquid interface, during the Cd^{2+} adsorption onto the composite materials, and also suggests that the systems present a disordered adsorption [15, 59]. The positive values of the standard enthalpy (ΔH^o) indicate that the Cd^{2+} adsorption on the three materials is endothermic. From the free enthalpy being much smaller than 80 kJ/mol we may conclude that the studied adsorption process is a physisorption. Above this value, the process is considered to be chemisorption [60].

In the same manner as the adsorption process, the ion exchange presumes the surface interaction of ionic species from an aqueous solution with a solid composite. Both of them are physical processes which are based on physical attractions, but they may be differentiated by the enthalpy values. Thus, in the case of ion exchange, the enthalpy value is much bigger compared with the adsorption process. The Cd^{2+} adsorption is an endothermic process, the ΔH^o values being positive and very small, indicating not strong electrostatic attractions [15,20,34,37,55,61-63]. Therefore for the present materials the process is adsorption and not ion exchange.

Nitrogen sorption data indicated that the specific surfaces areas decrease after the Cd^{2+} adsorption, which can be due to the Cd^{2+} adsorption into the pores.

8-4. Influence of Initial Concentration of the Cd(II)

The influence of Cd(II) initial concentration onto the nanocomposite materials adsorption capacity is depicted in Fig. 11. It can be observed that the increase of the initial concentration of Cd(II) leads to an increase of the adsorption capacity until a constant value is reached. Maximum value of the adsorption capacity has a value of 1.9 mg/g for 10-NC sample, 3.2 mg/g for 15-NC

Table 9. Thermodynamic parameters for the adsorption of Cd(II) onto materials

Temp, K	10-NC				15-NC				20-NC			
	K_d, L/g	ΔG^o, kJ/mol	ΔH^o, kJ/mol	ΔS^o, kJ/(mol K)	K_d, L/g	ΔG^o, kJ/mol	ΔH^o, kJ/mol	ΔS^o, kJ/(mol K)	K_d, L/g	ΔG^o, kJ/mol	ΔH^o, kJ/mol	ΔS^o, kJ/(mol K)
298	0.18	−2412.2			0.27	−1679.2			0.42	−1679.2		
308	0.19	−2604.5	3.31	19.85	0.31	−2115.4	10.45	38.47	0.5	−2115.5	11.32	43.62
318	0.19	−2796.7			0.36	−2551.7			0.58	−2551.7		

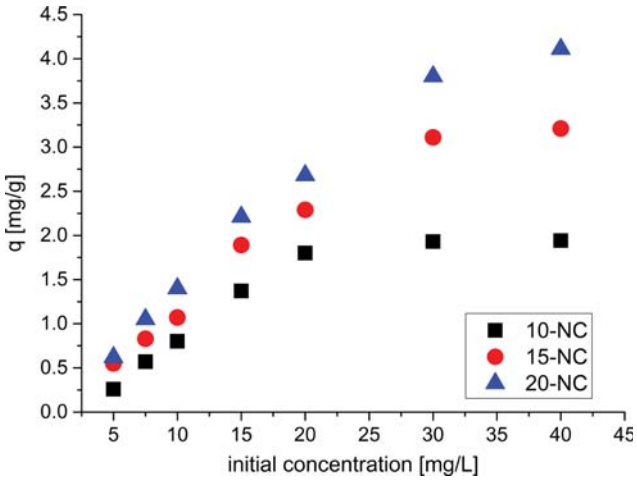

Fig. 11. Influence of the initial concentration of Cd(II) on the adsorption capacity of the nanocomposite materials. T=25 °C.

Table 10. Parameters of Langmuir and Freundlich isotherms for Cd(II) adsorption onto nanocomposite materials

	Parameters	10-NC	15-NC	20-NC
Adsorption isotherms		Experimental values		
	$q_{m,exp}$ (mg/g)	1.94	3.21	4.11
		Isotherm models' values		
Langmuir	q_L (mg/g)	1.97	3.71	4.48
	K_L (L/mg)	0.028	0.015	0.019
	R^2	0.9985	0.9549	0.9819
Freundlich	K_F (mg/g)	0.314	0.468	0.650
	$1/n_F$	0.558	0.621	0.615
	R^2	0.7554	0.8493	0.8818

sample and 4.1 mg/g for 20-NC sample in the present conditions with 30 mg Cd/L initial ion concentration. The maximum adsorption capacity values increase with the increase of the iron content in the materials. Thus, the composite material with the highest adsorption capacity is 20-NC. For the 0-NC sample with no iron content the adsorption capacities were low, and therefore equilibrium studies were not performed on this material. Previous studies proved that the co-presence of some other metal ions can decrease the adsorption capacity for Cd^{2+}, reducing therefore the composite's adsorption efficiency [64].

8-5. Adsorption Isotherms

Adsorption isotherms relate the solution concentration and the amount of sorbate adsorbed per unit mass of adsorbent at constant temperature. Langmuir and Freundlich equilibrium isotherms have been used to model the experimental data in order to establish the adsorption mechanism and the maximum adsorption capacity of the composite materials.

The adsorption isotherms of Cd(II) on the composite materials are presented in Fig, 12, and the fitted parameters with the correlation coefficients are collected in Table 8.

The adsorption process of Cd(II) on the composite materials is better described by the Langmuir model with regression coefficient in the range R^2=0.955-0.998. The maximum adsorption capacity theoretically obtained by modelling the experimental data with Langmuir isotherm (qL, exp, 10-NC=1.97 mg/g; qL, exp, 15-NC= 3.71 mg/g and qL, exp, 20-NC=4.48 mg/g) is very close to the experimental data values at the highest concentrations. Based on these results, it can be concluded that the adsorption process of Cd(II) on the composite materials is mono-layer adsorption on

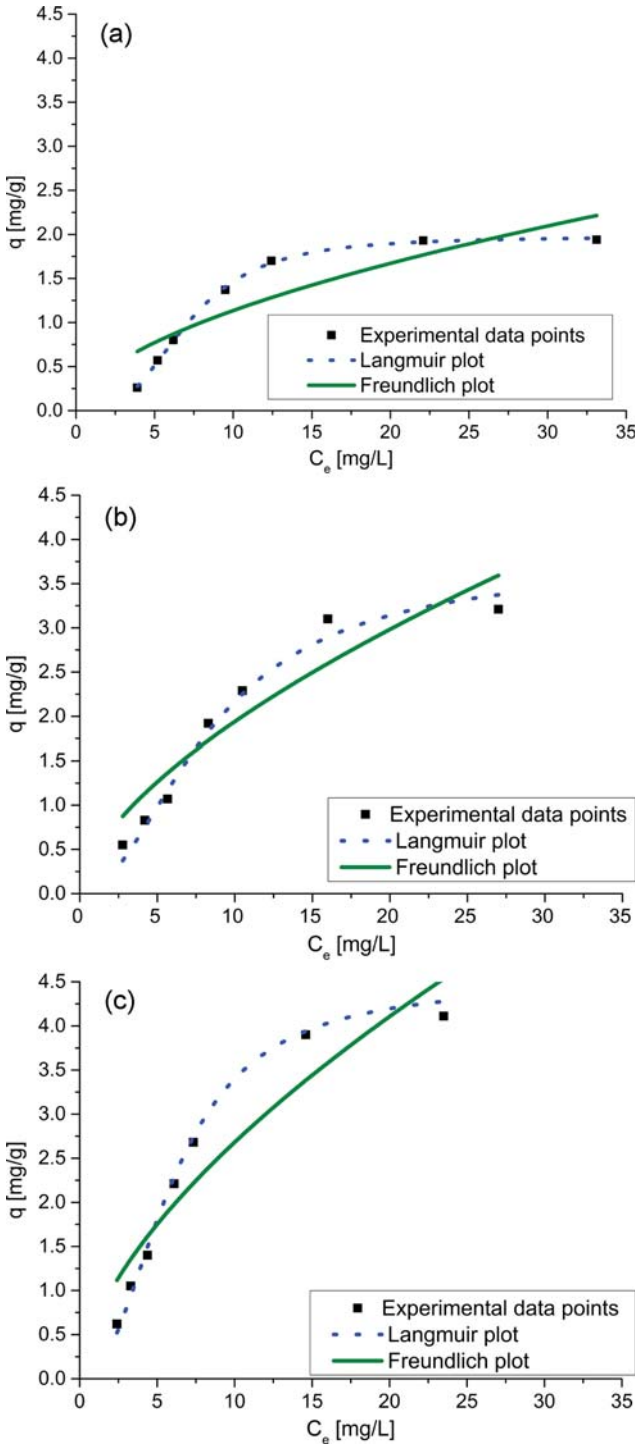

Fig. 12. Cd (II) adsorption isotherms of the composite materials. T=25 °C: (a) 10-NC, (b) 15-NC, (c) 20-NC.

the surface of the composite particles. The adsorption mechanism is controlled by chemisorption processes as a result of strong chelation between Cd(II) and iron oxides present on the composite materials surfaces. The linear representation of the Freundlich isotherm for all materials has very low correlation coefficients, suggesting that this isotherm cannot describe the Cd(II) adsorption onto the studied materials.

8-6. Regeneration Study

An important parameter for the characterization of the efficiency of the materials used as adsorbents is the regeneration capacity that may be translated as the property of materials of reutilization in the adsorption processes. One cycle (adsorption-desorption) of regeneration study was performed. The desorption was performed by mixing 1 g of cadmium containing composite mixed with 25 mL NaCl/HCl 5% solution and stirring for 2 h at 25 °C with 200 rpm stirring speed. Next, the material was filtered, washed with distilled water and dried at room temperature. The procedure of a previous study was followed [65].

The adsorption/desorption process may be represented as follows, from [61]:

$$H^+-R-H^+ + Cd^{2+} \rightleftharpoons R-Cd^{2+} + 2H^+ \quad (6)$$

The regeneration grade, for the three studied composites materials, was in the 90%-92% interval. Although, for the present study, only one cycle (adsorption-desorption) of regeneration study was performed, the high percent of regeneration obtained after the first cycle, shows its suitability for many regeneration cycles.

CONCLUSIONS

Composite silica materials containing magnetite or maghemite nanoparticles were prepared in a simple one-pot synthesis using PVA polymer as poroform and TEOS and $Fe(acac)_3$ precursors. Materials were characterized for their morphology and magnetic properties. Nitrogen adsorption revealed high surface area and total pore volume for all samples, and microporosity as major pore population. XRD and SANS indicated iron oxide nanoparticles with 20-30 nm dimensions. XRD shows also a gradual shift from hematite to magnetite depending on the iron content, supported also by Mössbauer data. Magnetic measurements show the highest value of saturation magnetization 54 emu/g.

To study the applicability of the composite materials the adsorption performance for cadmium removal was examined. The equilibrium data indicate predominantly monolayer adsorption on the composite's surfaces, and adsorption capacity in the range of 2-4 mg/g, after 120 min contact time, and increasing with the increase of the iron content. After evaluating the values of the regression coefficients, it can be concluded that the Cd^{2+} adsorption process onto the three studied materials is better fitted by the pseudo-second-order kinetic model. The negative values of the Gibbs free energy (ΔG^o) and the positive values of the standard enthalpy (ΔH^o) indicate that the Cd^{2+} adsorption on the three materials is a spontaneous and endothermic process. From the value of the standard enthalpy (much smaller than 80 kJ/mol) it resulted that the adsorption process is physisorption. Also, based on the better fit of the adsorption isotherms with the Langmuir model, it results that the adsorption mechanism is controlled by chemisorption processes, as a result of strong chelation between Cd(II) and iron oxides present on the composite materials surfaces. Therefore, we may conclude that for the present case, the adsorption mechanism is controlled by both physisorption and chemisorption processes. The regeneration grade, for the three studied composites materials, was in the 90%-92% interval after one adsorption-desorption cycle. The collected data indicate that the new produced materials can be used as adsorbents for recovery of metal ions from aqueous solutions.

ACKNOWLEDGEMENTS

The authors thank the Romanian Academy and the Inter-Academic Exchange Program between Academy of Sciences of the Czech Republic and Romanian Academy and the Inter-Academic Exchange Program between Romanian Academy and the Hungarian Academy of Sciences. Authors thank also Dr. Aurel Ercuta from West University of Timisoara, Romania for magnetic measurements and fruitful discussions.

REFERENCES

1. B. J. Clapsaddle, A. E. Gash, J. H. Satcher Jr. and R. L. Simpson, *J. Non-Cryst. Solids*, **331**, 190 (2003).
2. X. Ma, H. Tao, K. Yang, L. Feng, L. Cheng, X. Shi, Y. Li, L. Liu and Z. Guo, *Nano. Res.*, **5**, 199 (2012).
3. C. Ianăşi, O. Costişor, A. M. Putz, J. Plocek, L. Săcărescu, D. Nižňanský and C. Savii, *Curr. Org. Chem.*, **21**, 2783 (2017).
4. C. Chanéac, E. Tronc and J. P. Jolivet, *J. Mater. Chem.*, **6**, 1905 (1996).
5. W. Wei, J. Changzhong and A. L. R. Vellaisamy, *Nanoscale*, **7**, 38 (2015).
6. R. R. Pawar, L. M. Kim, J. G. Kim, S. M. Hong, S. Y. Sawant and S. M. Lee, *Appl. Clay Sci.*, **162**, 339 (2018).
7. S. K. R. Yadanaparthi, D. Graybill and R. Wandruszka, *J. Hazard. Mater.*, **171**, 1 (2009).
8. S. Behrens, *Nanoscale*, **3**, 877 (2011).
9. B. Julián-López, C. Boissière, C. Chanéac, D. Grosso, S. Vasseur, S. Miraux, E. Duguet and C. Sanchez, *J. Mater. Chem.*, **17**, 1563 (2007).
10. D. L. Leslie-Pelecky and R. D. Rieke, *Chem. Mater.*, **8**, 1770 (1996).
11. S. Solinas, G. Piccaluga, M. P. Morales and C. J. Serna, *Acta Mater.*, **49**, 2805 (2001).
12. R. Ullah, B. D. Kumer and Y. A. M. Mohammad, *Int. J. Compos. Mater.*, **4**, 135 (2014).
13. D. Li, W. Y. Teoh, R. C. Woodward, J. D. Cashion, C. Selomulya and R. Amal, *J. Phys. Chem. C*, **113**, 12040 (2009).
14. S. H. Kang, J. Lee and J. H. Chang, *J. Phys. Chem. C*, **114**, 12440 (2010).
15. M. Naushad, Z. A. AL-Othman and M. Islam, *Int. J. Environ. Sci. Technol.*, **10**, 567 (2013).
16. M. Naushad, Inamuddin and T. A. Rangreez, *Desalin. Water Treat.*, **55**, 463 (2014).
17. M. Naushad, A. Mittal, M. Rathore and V. Gupta, *Desalin. Water Treat.*, **54**, 2883 (2015).
18. J. K. Beadinko, W. Wei and Y. S. Yun, *J. Ind. Eng. Chem.*, **43**, 61 (2016).
19. E. Fosso-Kankeu, H. Mittal, F. Waanders and S. S. Ray, *J. Ind. Eng.*

Chem., **48**, 151 (2017).
20. M. Naushad, T. Ahamad, Z. A. AL-Othman, M. A. Shar, N. S. Al Hokbany and S. M. Alshehri, *J. Ind. Eng. Chem*., **29**, 78 (2015).
21. M. Naushad, A. Mittalb, M. Rathorec and V. Gupta, *Desalin. Water Treat*., **54**, 1 (2014).
22. R. Hlihor and M. Gavrilescu, *Environ. Eng. Manag. J*., **8**, 353 (2009).
23. L. Sailo, L. Pachuau, J. K. Yang, S. M. Lee and D. Tiwari, *Environ. Eng. Res*., **20**, 89 (2015).
24. R. R. Pawar, H. A. Patel, G. Sethia and H. C. Bajaj, *Appl. Clay Sci*., **46**, 109 (2009).
25. M. Bystrzejewski, K. Pyrzyńska, A. Huczko and H. Lange, *Carbon*, **47**, 1189 (2009).
26. T. Phuengprasop, J. Sittiwong and F. Unob, *J. Hazard. Mater*., **186**, 502 (2011).
27. M. Zhang, W. Song, Q. Chen, B. Miao and W. He, *ACS Appl. Mater. Interfaces*, **7**, 1533 (2015).
28. W. Zheng, X. Li, F. Wang, Q. Yang, P. Deng and G. Zeng, *J. Hazard. Mater*., **157**, 490 (2008).
29. L. Rosta, *Appl. Phys. A*, **74**, S52 (2002).
30. I. Mihalca and A. Ercuta, *J. Optoelectron. Adv. Mater*., **5**, 245 (2003).
31. B. Pal and M. Sharon, *Thin Solid Films*, **379**, 83 (2000).
32. S. N. Slabzhennikov, O. B. Ryabchenko and L. A. Kuarton, *Russ. J. Coord. Chem*., **29**, 484 (2003).
33. C. Ianăşi, O. Costisor, A. M. Putz, R. Lazau, A. Negrea, D. Niznansky, L. Sacarescu and C. Savii, *Process. Appl. Ceram*., **10**, 265 (2016).
34. M. Waseem, S. Mustafa, A. Naeem, G. J. M. Koper and K. H. Shah, *Desalination*, **277**, 221 (2011).
35. M. Benhaliliba, C. E. Benouis and A. S. Tiburcio, *J. Lumin*., **132**, 2653 (2012).
36. K. Kaviyarasu, E. Manikandan, P. Paulraj, S. B. Mohamed and J. Kennedy, *J. Alloy Compd*., **593**, 67 (2014).
37. S. Mustafa, M. Waseem, A. Naeem, K. H. Shah and T. Ahmad, *Desalination*, **255**, 148 (2010).
38. M. Thommes, K. Kaneko, A. V. Neimark, J. P. Olivier, F. Rodriguez-Reinoso, J. Rouquerol and K. S. W. Sing, *Pure Appl. Chem*., **87**, 1051 (2015).
39. S. Lowell, J. E. Shields, M. A. Thomas and M. Thommes, Characterization of Porous Solids and Powders: Surface Area, Pore Size and Density, Springer Science-Business Media, New York (2004).
40. R. Haul and T. Schoon, *Z. Phys. Chem*., **44**, 216 (1939).
41. M. Y. Antipin, V. G. Tzirelson, M. P. Flugge, R. G. Gerr, Y. T. Struchkov and R. P. Ozerov, *Dokl. Akad. Nauk SSSR*, **281**, 854 (1985).
42. P. S. Sidhu, *Clays Clay Miner*., **36**, 31 (1988).
43. R. Gruskiene, T. Krivorotova, R. Staneviciene, D. Ratautas, E. Serviene and J. Sereikaite, *Colloids Surf., B*., **8**, 126 (2018).
44. G. M. S. el Shafei, Adsorption on Silica Surfaces, Marcel Dekker, New York (2000).
45. T. V. Nagorna, O. A. Kyzyma, D. Chudoba and A. V. Nagornyi, *J. Mol. Liq*., **235**, 111 (2017).
46. C. Savii, L. Almásy, C. Ionescu, N. K. Székely, C. Enache, M. Popovici, I. Sora, D. Nicoara, G. G. Savii, D. S. Resiga, J. Subrt and V. Štengl, *Process. Appl. Ceram*., **3**, 59 (2009).
47. A Guinier and G. Fournet, Small angle scattering of X-rays, John Wiley and Son, New York (1955).
48. L. Almasy, A. M. Putz, A. Len, J. Plestil and C. Savii, *Process. Appl. Ceram*., **11**, 229 (2017).
49. Z. Dudás, E. Fagadar-Cosma, A. Len, L. Románszki, L. Almásy, B. Vlad-Oros, D. Dascălu, A. Krajnc, M. Kriechbaum and A. Kuncser, *Materials*, **11**, 565 (2018).
50. E. Fagadar-Cosma, Z. Dudas, M. Birdeanu and L. Almasy, *Mater. Chem. Phys*., **148**, 143 (2014).
51. N. N. Gubanova, A. Ye. Baranchikov, G. P. Kopitsa, L. Almásy, B. Angelov, A. D. Yapryntsev, L. Rosta and V. K. Ivanov, *Ultrason. Sonochem*., **24**, 230 (2014).
52. A. T. Goulart, M. F. de Jesus Filho, J. D. Fabris and J. M. D. Coey, *Hyperfine Interact*., **83**, 451 (1994).
53. I. Langmuir, *J. Am. Chem. Soc*., **40**, 1361 (1918).
54. H. M. F. Freundlich, *J. Phys. Chem*., **57**, 385 (1906).
55. S. Mustafa, M. Waseem, A. Naeem, K. H. Shah, T. Ahmad and S. Y. Hussain, *Chem. Eng. J*., **157**, 18 (2010).
56. I. Llorente, S. Fajardo and J. M. Bastidas, *J. Solid State Electrochem*., **18**, 293 (2014).
57. M. Ghasemi, M. Naushad, N. Ghasemi and Y. Khosravi-fard, *J. Ind. Eng. Chem*., **20**, 2193 (2014).
58. V. S. Markin, M. I. Gugeshashvili, A. G. Volkov, G. Munger and R. M. Leblanc, *J. Colloid Interface Sci*., **154**, 264 (1992).
59. Z. A. AL-Othman, R. Ali and M. Naushad, *Chem. Eng. J*., **184**, 238 (2012).
60. S. Chowdhury, R. Mishra, P. Saha and P. Kushwaha, *Desalination*, **265**, 159 (2011).
61. M. Naushad, *Chem. Eng. J*., **235**, 100 (2014).
62. M. Naushad, T. Ahamad, G. Sharma, Ala'a H. Al-Muhtaseb, A. B. Albadarin, M. M. Alam, Z. A. AL-Othman, S. M. Alshehri and A. A. Ghfar, *Chem. Eng. J*., **300**, 306 (2016).
63. M. Naushad, T. Ahamad, B. M. Al-Maswari, A. A. Alqadami and S. M. Alshehri, *Chem. Eng. J*., **330**, 1351 (2017).
64. A. Negrea, C. Muntean, I. Bodnarescu, M. Ciopec and M. Motoc, *Rev. Chim*., **64**, 397 (2013).
65. M. Ciopec, C. M. Davidescu, A. Negrea, N. Duțeanu, G. Rusu, O. Grad and P. Negrea, *Pure Appl. Chem*., **91**, 375 (2018).